PEELING CONTEXT FROM CAUSE FOR MULTIMODAL MOLECULAR PROPERTY PREDICTION

Tao Li, Kaiyuan Hou & Tuan Vinh
Department of Computer Science
Emory University
Atlanta, GA 30322, United States
{tli349, khou6, tvinh}@emory.edu

Carl Yang & Monika Raj
Computer Science, Chemistry
Emory University
Atlanta, GA 30322, United States
{ jyang71, mraj4}@emory.edu

ABSTRACT

Deep models are used for molecular property prediction, yet they are often hard to interpret and may rely on spurious context rather than causal structure, which degrades reliability under distribution shift and harms predictive performance. We introduce **CLaP**, *Causal Layerwise Peeling*, a framework which separates causal signal from context in a layerwise manner and integrates diverse graph representations of molecules. At each layer, a *causal block* performs a soft split into causal and trivial branches, fuses causal evidence across modalities, and progressively *peels* batch-coupled context to concentrate on label-relevant structure, thereby limiting shortcut signals and stabilizing layerwise refinement. Across four molecular benchmarks, CLaP reliably improves MAE, MSE, and R^2 over competitive baselines. We also obtain atom-level causal saliency maps that highlight substructures responsible for a prediction, providing actionable guidance for targeted molecular edits. Case studies confirm the accuracy of these maps and their alignment with chemical intuition. By peeling context from cause at every layer, the model delivers predictors that are accurate and interpretable for molecular design.

1 Introduction

Designing molecules with desired properties is a central goal in drug discovery and materials design (Sanchez-Lengeling & Aspuru-Guzik, 2018). Graph-based deep learning is effective for property prediction (Wu et al., 2018; Hinton et al., 2006; Bengio & LeCun, 2007; Goodfellow et al., 2016). However, models often exploit spurious correlations tied to datasets or batches (Geirhos et al., 2020), which hurts reliability under distribution shift. They also provide limited substructure-level guidance (Jiménez-Luna et al., 2020), reducing their value for design. These gaps motivate predictors that separate causal signal from contextual shortcuts and yield chemically meaningful attributions.

Prior work on invariant rationales (e.g., DIR, CAL) promotes causal subgraphs by enforcing invariance across *constructed* environments (Wu et al., 2022; Sui et al., 2022; Chen et al., 2022). While influential, these approaches are largely designed for classification, rely on synthetic environments whose fidelity to real data is uncertain, and often treat causality as a one-shot selection problem. We take a different route and introduce **CLaP**, *Causal Layerwise Peeling*, a layerwise framework that peels context from cause. At each layer, a learnable splitter routes features into a *causal* branch and a *trivial* branch, progressively *peeling* batch-coupled context and concentrating on label-relevant structure. Rather than engineering synthetic environments (e.g., graph perturbations) or selecting a sparse subgraph with a predictor trained to be stable across them, we exploit the natural fluctuations of ordinary mini-batches during training as contextual variation that the model learns to ignore.

Our design is grounded in a *batch-wise invariance* principle. As batch composition changes during training, only sample intrinsic signal should keep a stable alignment with the label. We implement this with a depth dependent correlation target and a monotonicity regularizer. The causal readout increases its within batch Pearson correlation with the label from shallow to deep layers. A stop gradient residual objective trains the trivial branch on the remaining error. This enforces a clean division of labor and prevents shortcut leakage into the causal path. Building on this premise, we formulate a *regression-ready* objective that aligns the scalar causal readout with continuous labels

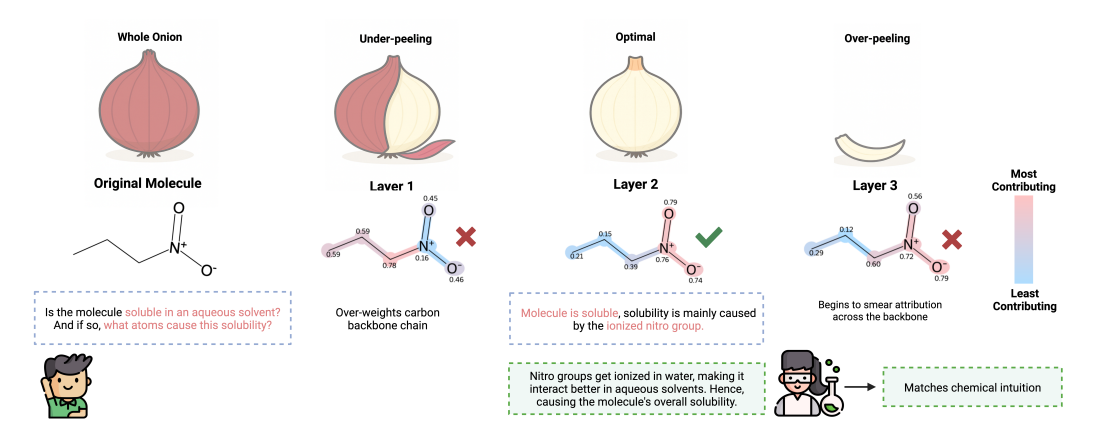


Figure 1: The original molecule in this illustrative example is iteratively "peeled" across layers. At shallow layers (layer 1), attribution underpeels and overweighs the carbon backbone. At the optimal layer, causal weights concentrate on the nitro group, yielding chemically plausible solubility drivers. Deeper peeling begins to smear attribution across the backbone, reflecting over-peeling in practice.

and enforces non-decreasing correlation across depth. These design choices enable CLaP to *peel* context from cause without synthetic environments and to provide robust, interpretable predictions.

From a molecular-property standpoint, different representations usually capture complementary facets of the same molecule. We therefore fuse same-depth causal evidence from three views—2D topology (SMILES graphs), peptide notation (HELM (Zhang et al., 2012)), and 3D geometry. A learned gating module assigns sample-specific weights, up-weighting the modality that carries batch-invariant signal at each layer. Gating weights yield atom-level causal saliency maps, and layerwise fusion peels away context to reveal the label-driving substructures (see Fig. 1).

Experiments on small-molecule benchmarks (ESOL, FreeSolv, Lipo) and cyclic peptides (CycPeptMPDB) show CLaP achieves consistent gains in MAE, MSE, and R^2 over architecture-centric baselines (MAT, FP-GNN) and causality-oriented baselines (DIR, CAL) (Maziarka et al., 2019; Cai et al., 2022; Wu et al., 2022; Sui et al., 2022). The atom-level saliency maps align with chemical intuition and, in case studies, pinpoint causal patterns and suggest targeted molecular edits.

In conclusion, our contributions are as follows:

- We propose CLaP, a multimodal, layerwise framework that splits features into *causal* and *trivial* branches at every layer and fuses same layer causal evidence across molecular views, reducing reliance on datasets or batches specific shortcuts, enhancing causality.
- CLaP produces causal saliency maps that highlight label-critical substructures. In case studies, these maps match chemical intuition and provide guidance for molecular design.
- Across diverse molecular property datasets, CLaP surpasses strong baselines. Its causal—trivial split reduces reliance on spurious context, improving robustness and accuracy.

2 METHODOLOGY

We first formalize a *batch-wise invariance* principle that provides the theoretical basis for our supervised causal objective. We then instantiate it with a layerwise causal–trivial architecture that fuses modalities and splits features per layer to enable both causal alignment and interpretability.

2.1 BATCH-WISE INVARIANCE

During training, each molecule is repeatedly sampled into different mini-batches across epochs, and thus encounters varying *batch contexts* defined by the co-occurring samples and their label statistics. A reliable predictor should maintain consistent alignment with the ground-truth label regardless of such batch fluctuations. This observation motivates a *batch-wise invariance* principle: only sample-intrinsic signal can sustain stable correlation with the label under changing batch contexts.

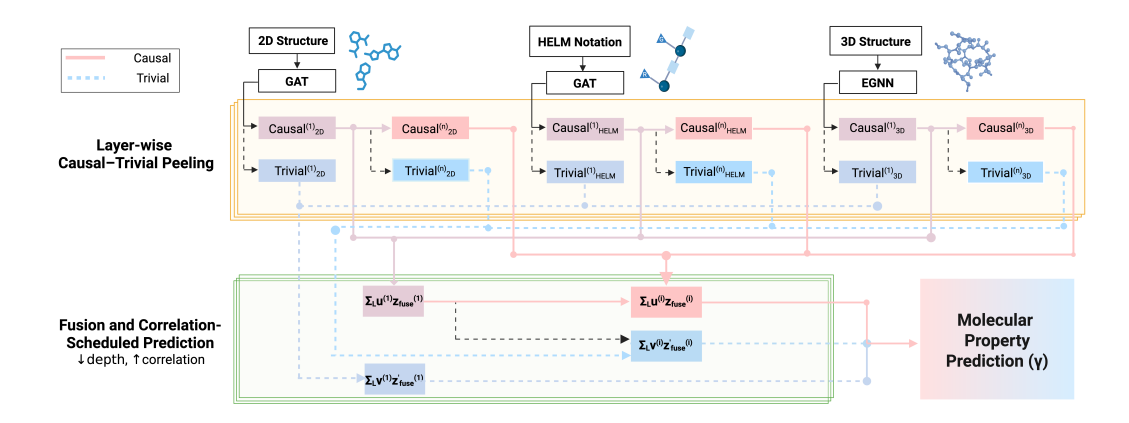


Figure 2: Overview of the causal layerwise peeling architecture for L=2 layers.

Setup. Index mini-batches by $e \in \mathcal{E}$ over random shuffles. Assume an additive view of the label

$$y = \theta c(x) + \eta, \qquad \mathbb{E}[\eta \mid x] = 0, \tag{1}$$

where c(x) is a sample-intrinsic, label-relevant component. Let q(x,e) denote *context* features whose association with y may *depend on* the batch e. Consider a local linearization of a layer's scalar predictor with scalars a, b.

$$s(x,e) = a c(x) + b q(x,e), \tag{2}$$

Batchwise correlation. For any batch e of size B_e , define batch-centered variables

$$\widetilde{u}_e = u - \frac{1}{B_e} (\mathbf{1}^\top u) \mathbf{1},$$

and the within-batch Pearson correlation

$$\operatorname{Corr}_{e}(u,v) = \frac{\langle \widetilde{u}_{e}, \widetilde{v}_{e} \rangle}{\|\widetilde{u}_{e}\|_{2} \|\widetilde{v}_{e}\|_{2} + \varepsilon}, \qquad \varepsilon > 0 \text{ small.}$$
(3)

Invariance objective. Batch-wise invariance requires

$$\operatorname{Corr}_{e}(s(x, e), y) \approx \rho \quad \text{for all } e \in \mathcal{E}, \text{ fixed } \rho \in [-1, 1].$$
 (4)

i.e., small dispersion of $Corr_e(s, y)$ across changing batches. A convenient surrogate is

$$\min_{a,b} \sum_{e \in \mathcal{E}} \left(\operatorname{Corr}_e(s(x,e), y) - \rho \right)^2. \tag{5}$$

Assumption. We make the following assumptions:

- A1. $\operatorname{Corr}_{e}(c(x), y) = \kappa$ is constant in e (sample-intrinsic stability).
- A2. $Corr_e(q(x, e), y)$ varies with e (batch-sensitive context).
- A3. $\operatorname{Var}_e(c(x))$ and $\operatorname{Var}_e(q(x,e))$ are bounded away from 0.

Then any predictor of the form equation 2 that satisfies the batch-wise invariance requirement equation 4 for all $e \in \mathcal{E}$ must have b=0. Equivalently, the batch-invariant solution discards q and retains c, and $\mathrm{Corr}_e(s,y)=\mathrm{Corr}_e(c,y)=\kappa$ for all e. A proof for invariance is provided in Appendix A.1.

2.2 LAYER-WISE CAUSAL-TRIVIAL PEELING

Our framework integrates three molecular views—2D graphs (SM), HELM notations (PE), and 3D geometries (GE). At each layer, causal blocks softly split features into *causal* and *trivial* paths. Causal signals are fused across modalities and aligned with the label via a depth-wise correlation schedule, while residual context is peeled and accumulated with stop-gradient. The final prediction combines the last causal readout and the accumulated residual (see Fig. 2).

Causal block. From the modality-specific node embeddings produced by the backbone encoders, each block at depth $\ell \in \{1,\dots,L\}$ applies a learnable node-wise splitter that assigns every atom/group a causal gate $\alpha_c^{(\ell)} \in [0,1]$. Its complement $\alpha_t^{(\ell)} = 1 - \alpha_c^{(\ell)}$ acts as the trivial gate. These gates induce two branches per modality: a causal representation $z_c^{(\ell)}$ and a trivial representation $z_t^{(\ell)}$. For each modality at depth ℓ , we obtain causal vectors $z_{SM}^{(\ell)}$, $z_{PE}^{(\ell)}$, $z_{GE}^{(\ell)} \in \mathbb{R}^D$ from the current block, along with the trivial vectors $z_{SM}^{(\ell)}$, $z_{PE}^{\prime(\ell)}$, $z_{GE}^{\prime(\ell)} \in \mathbb{R}^D$. A gating network $g_F(\cdot)$ produces sample-specific soft weights $w^{(\ell)}$ over modalities via a softmax, and these weights are used to form the fused causal representation $z_{fuse}^{(\ell)}$ (and the fused trivial representation $z_{fuse}^{\prime(\ell)}$) at depth ℓ .

$$oldsymbol{w}^{(\ell)} = \operatorname{softmax} \Big(g_F \big([oldsymbol{z}_{SM}^{(\ell)}; oldsymbol{z}_{PE}^{(\ell)}; oldsymbol{z}_{GE}^{(\ell)}] \big) / au \Big) \in \mathbb{R}^3,$$

Scalar readouts use projection heads. Applying causal head $\boldsymbol{u}^{(\ell)}$ to $\mathbf{z}_{\mathit{fuse}}^{(\ell)}$ yields $\boldsymbol{c}^{(\ell)}$, while applying trivial head $\boldsymbol{v}^{(\ell)}$ to $\mathbf{z}_{\mathit{fuse}}^{\prime(\ell)}$ yields $\boldsymbol{t}^{(\ell)}$. The causal branch is forwarded to depth $\ell+1$ (yielding $\boldsymbol{c}^{(\ell+1)}$) while an additional trivial component $t^{(\ell+1)}$ is peeled. This recursion continues until depth L.

After block L, the per-batch scalars are stacked across layers to enable supervision and analysis.

$$oldsymbol{C} = ig[oldsymbol{c}^{(1)} \cdots oldsymbol{c}^{(L)}ig], \qquad oldsymbol{T} = ig[oldsymbol{t}^{(1)} \cdots oldsymbol{t}^{(L)}ig] \ \in \mathbb{R}^{B imes L}.$$

Causal branch: depth-guided correlation. The causal branch is designed to focus, layerwise, on the label-predictive signal. At each depth ℓ , we align the fused causal scalar $e^{(\ell)}$ with the batch labels $y \in \mathbb{R}^B$ by *constraining* their Pearson correlation to follow a depth-dependent target schedule.

We first center the variables and then calculate the mini-batch Pearson correlation at depth ℓ with a small stabilizer $\epsilon > 0$.

$$\widetilde{\boldsymbol{c}}^{(\ell)} = \boldsymbol{c}^{(\ell)} - \frac{1}{B} (\mathbf{1}^{\top} \boldsymbol{c}^{(\ell)}) \mathbf{1} \qquad \widetilde{\boldsymbol{y}} = \boldsymbol{y} - \frac{1}{B} (\mathbf{1}^{\top} \boldsymbol{y}) \mathbf{1},
\operatorname{corr}_{\ell} = \frac{\langle \widetilde{\boldsymbol{c}}^{(\ell)}, \widetilde{\boldsymbol{y}} \rangle}{\|\widetilde{\boldsymbol{c}}^{(\ell)}\|_{2} \|\widetilde{\boldsymbol{y}}\|_{2} + \epsilon} \in [-1, 1].$$
(6)

We set a linearly increasing target correlation schedule so that deeper layers are encouraged to capture progressively finer, label-critical variation:

$$\rho_{\ell} = \rho_{\min} + \frac{\ell - 1}{L - 1} \left(\rho_{\max} - \rho_{\min} \right), \qquad \ell = 1, \dots, L.$$
(7)

Then penalize deviations between the batchwise Pearson correlation and its target,

$$\mathcal{L}_{\text{corr}} = \frac{1}{L} \sum_{\ell=1}^{L} \left(\text{corr}_{\ell} - \rho_{\ell} \right)^{2}, \tag{8}$$

The correlation loss guides each layer toward the target depth-wise trend and concentrates causal signal while filtering out irrelevant batch-specific context noise.

To stabilize the hierarchy and prevent causal regression from ℓ to $\ell+1$, we further apply a monotonicity regularizer, encouraging correlations to be non-decreasing from layer to layer via a hinge penalty with margin $\gamma \ge 0$:

$$\mathcal{L}_{\text{mono}} = \frac{1}{L-1} \sum_{\ell=1}^{L-1} \max \left\{ 0, \operatorname{corr}_{\ell} - \operatorname{corr}_{\ell+1} + \gamma \right\}. \tag{9}$$

Together, equation 8—equation 9 encourage a depth-wise progression. Shallow layers capture coarse, high-variance patterns, and deeper layers increasingly model causal patterns.

Trivial branch: residual learning. The trivial branch isolates context and irrelevant variation that are not central to prediction. By removing these factors from the causal branch, the causal signal becomes clearer and more discriminative. At depth ℓ , each block yields a trivial scalar $t^{(\ell)}$. We aggregate these across layers, while retaining only the final causal scalar as the causal output:

$$t = \sum_{\ell=1}^{L} \boldsymbol{t}^{(\ell)} \in \mathbb{R}^{B}, \qquad y_{c}^{\star} = \boldsymbol{c}^{(L)}. \tag{10}$$

To maintain a clear division of labor, the trivial branch is trained on the residual between the ground-truth label y and the final causal output, with gradients stopped through y_c^* to avoid contaminating the causal pathway:

$$\mathcal{L}_{\text{triv}} = \text{MSE}(t, \ \boldsymbol{y} - \text{stopgrad}(\boldsymbol{y}_{c}^{\star})).$$
 (11)

This design assigns the stable, generalizable component to the causal path, whereas the trivial path captures the remaining residual variation, calibrating y_c^{\star} by absorbing context-specific noise that should not be attributed to the causal branch.

Prediction and total objective. The model predicts by additively combining the depth-L causal readout with the accumulated trivial correction:

$$\hat{y} = y_c^* + t, \qquad \mathcal{L}_{pred} = MSE(\hat{y}, y).$$
 (12)

We regularize the causal branch toward *batch-invariant*, depth-increasing alignment with the label, while training the trivial branch on the residual (with stop–gradient on y_c^*). The full objective is

$$\mathcal{L}_{\mathrm{total}} = \mathcal{L}_{\mathrm{pred}} + \underbrace{\lambda_{\mathrm{caus}}\,\mathcal{L}_{\mathrm{corr}}}_{\text{causal alignment}} + \underbrace{\lambda_{\mathrm{mono}}\,\mathcal{L}_{\mathrm{mono}}}_{\text{depth monotonicity}} + \underbrace{\lambda_{\mathrm{unif}}\,\mathcal{L}_{\mathrm{triv}}}_{\text{residual fit}}, \quad \lambda_{\mathrm{caus}}, \lambda_{\mathrm{mono}}, \lambda_{\mathrm{unif}} \geq 0.$$

3 EXPERIMENTS

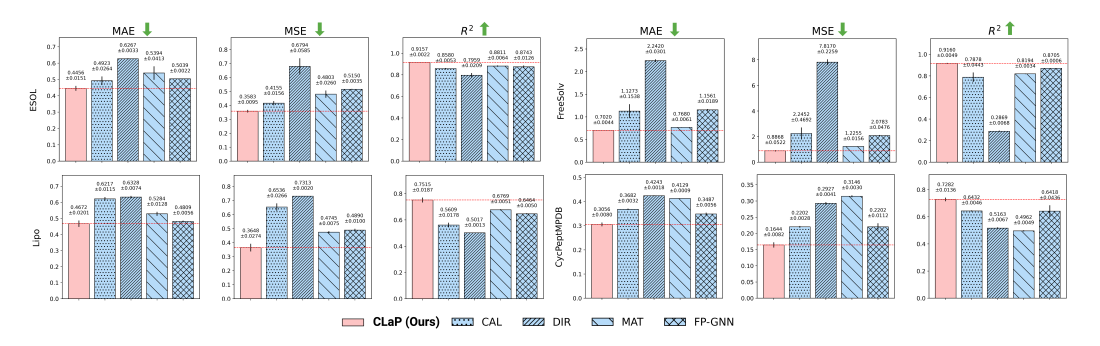


Figure 3: Performance comparison across four molecular property datasets.

3.1 Experimental Settings

Datasets. We evaluate CLaP on four publicly available benchmark datasets: *ESOL*, a *widely used* dataset of aqueous solubility values; *FreeSolv*, reporting experimentally measured hydration free energies of small molecules; and *Lipo*, containing curated standard octanol/water distribution coefficients; *CycPeptMPDB*, which measures *passive* cell permeability of cyclic peptides.

Baselines. We compare against two representative categories of methods: (i) *architecture-centric* models that focus on network design for molecular property prediction, including MAT (Maziarka et al., 2019) (Molecule Attention Transformer) and FP-GNN (Cai et al., 2022) (Fingerprints and Graph Neural Networks); and (ii) *causality-oriented* approaches that aim to improve prediction by explicitly modeling causal structures or mitigating confounding, including DIR (Wu et al., 2022) (Discovering Invariant Rationales) and CAL (Sui et al., 2022) (Causal Attention Learning). For causality-oriented models originally designed for classification, we retain their core architectures and modify only the output head to perform regression (i.e., single-scalar prediction), preserving their causal mechanisms unchanged. See Appendix D.2 for further implementation details.

3.2 MAIN RESULTS

Figure 3 summarizes the overall comparative regression performance on four molecular property datasets. CLaP consistently achieves the best MAE, MSE, and R^2 across all benchmarks. Notably, CycPeptMPDB, the most challenging benchmark due to its focus on peptide permeability, CLaP achieves a 17.0% lower MAE and 25.4% lower MSE compared to the best baseline (FP-GNN), along with an absolute R^2 improvement of 8.6 points. Empirically, this collectively highlights the strong advantage of our causal–trivial peeling under complex structure–property confounding.

Beyond CycPeptMPDB, CLaP achieves consistent improvement on *ESOL*, *FreeSolv*, and *Lipo*, outperforming prior architectures and causality-based models in accuracy and correlation metrics, especially on *FreeSolv*, where data scarcity (\sim 600 samples) limits performance. These results further demonstrate our design's generalizability across molecular size, data regime, and property type.

3.3 VARIANTS AND ABLATIONS

Table 1: Ablation study on framework design across four datasets.

Setting	MAE	MSE	R^2	
ESOL				
CLaP	0.4456 ± 0.0151	0.3583 ± 0.0095	0.9157 ± 0.0022	
w/o causal-trivial split	0.5094 ± 0.0528	0.4939 ± 0.1303	0.8838 ± 0.0243	
w/o correlation schedule	0.5078 ± 0.0190	0.4767 ± 0.0677	0.8879 ± 0.0159	
w/o trivial branch	0.4732 ± 0.0210	0.4137 ± 0.0253	0.9059 ± 0.0093	
	FreeSo	olv		
CLaP	0.7020 ± 0.0044	0.8866 ± 0.0522	0.9160 ± 0.0049	
w/o causal-trivial split	1.2858 ± 0.2120	2.5719 ± 0.8194	0.7562 ± 0.0777	
w/o correlation schedule	0.8779 ± 0.1003	1.3742 ± 0.0433	0.8697 ± 0.0041	
w/o trivial branch	1.0753 ± 0.0593	1.7338 ± 0.2021	0.8356 ± 0.0919	
	Lipa)		
CLaP	0.4672 ± 0.0020	0.3645 ± 0.0274	0.7515 ± 0.0187	
w/o causal-trivial split	0.5145 ± 0.0425	0.4302 ± 0.0242	0.7240 ± 0.0062	
w/o correlation schedule	0.5562 ± 0.0195	0.5122 ± 0.0420	0.6508 ± 0.0282	
w/o trivial branch	0.5824 ± 0.0200	0.5348 ± 0.0115	0.6292 ± 0.0072	
CycPeptMPDB				
CLaP	0.3056 ± 0.0080	0.1644 ± 0.0082	0.7282 ± 0.0136	
w/o causal-trivial split	0.3120 ± 0.0047	0.1834 ± 0.0063	0.6969 ± 0.0104	
w/o correlation schedule	0.3215 ± 0.0068	0.1866 ± 0.0087	0.6917 ± 0.0144	
w/o trivial branch	0.3214 ± 0.0012	0.2037 ± 0.0116	0.6634 ± 0.0192	

3.3.1 Framework design

Table 1 reports ablations of core framework components. The full model integrates the depthwise correlation schedule (Eq. equation 8) and a stop–gradient trivial branch (Eq. equation 11).

w/o causal-trivial split. This variant removes the correlation loss $\mathcal{L}_{\mathrm{corr}}$, the trivial loss $\mathcal{L}_{\mathrm{triv}}$, and the monotonicity penalty $\mathcal{L}_{\mathrm{mono}}$, thereby collapsing our two-branch design. Training reduces to plain regression with $\mathcal{L}_{\mathrm{pred}}$ (Eq. equation 12). Empirically, performance drops (e.g., on the CycPeptMPDB dataset, R^2 drops from 0.728 to 0.697), indicating that straightforward end-to-end fitting struggles to separate label-relevant structure and is easily distracted by spurious information.

Under the batch-wise invariance view, a predictor that mixes batch-dependent context q(x,e) with intrinsic signal c(x) yields $\operatorname{Corr}_e(s,y)$ that fluctuates with e. Removing the split collapses the losses $\mathcal{L}_{\operatorname{corr}}, \mathcal{L}_{\operatorname{triv}}, \mathcal{L}_{\operatorname{mono}}$, allowing $b \neq 0$ in Eq. equation 2, contradicting the invariant solution driven by Eq. equation 5. The performance drop reflects increased reliance on batch-sensitive shortcuts.

w/o correlation schedule. We omit the correlation loss \mathcal{L}_{corr} and (Eq. equation 8), which disables the target schedule for ρ . The depth schedule $\{\rho_\ell\}$ (Eq. equation 7) and \mathcal{L}_{corr} (Eq. equation 8) specify a curriculum from coarse to decisive label-relevant factors.

Without this schedule, the stack lacks directional guidance and drifts toward batch-specific shortcuts. It fits residual patterns with little label signal, which hurts generalization. Keeping the monotonicity term $\mathcal{L}_{\mathrm{mono}}$ is not enough because the non-decreasing constraint lacks direction and cannot steer

which features to keep or discard. In the full model the schedule works as a curriculum that allocates capacity to increasingly predictive components and focuses deeper layers on label relevant variation.

w/o trivial branch. We ablate the trivial branch and predict solely from the final-layer causal output y_c^{\star} . This forces residual context into the causal branch and eliminates residual calibration of environment-driven variation, causing *leakage* of non-causal factors and a performance drop. See Appendix A.2 for a formal derivation and risk decomposition.

For instance, in a testing example with ground-truth permeability y=-0.80, we observe $y_{\rm c}^{\star}=-0.78$ and t=-0.01, yielding a final prediction $\widehat{y}=y_{\rm c}^{\star}+t=-0.79$. This decomposition reflects how $y_{\rm c}^{\star}$ captures the stable, mechanism-driven component, while t calibrates a small, context-dependent bias. Without the trivial head, however, such residual calibration becomes unavailable. The model is forced to encode both signals into $y_{\rm c}^{\star}$, entangling causal and contextual information.

Setting	MAE	MSE	R^2
	Peel	ling Depth(L)	
3	0.3265 ± 0.0044	0.1903 ± 0.0044	0.6854 ± 0.0073
5	0.3056 ± 0.0080	$\textbf{0.1644} \pm \textbf{0.0082}$	$\textbf{0.7282} \pm \textbf{0.0136}$
7	0.3296 ± 0.0007	0.2020 ± 0.0015	0.6662 ± 0.0025
9	0.3297 ± 0.0070	0.1875 ± 0.0077	0.6902 ± 0.0127
	Peeling	g Strength $(ho_{ m max})$	
0.60	0.3131 ± 0.0075	0.1741 ± 0.0097	0.7123 ± 0.0161
0.70	0.3162 ± 0.0040	0.1733 ± 0.0053	0.7137 ± 0.0088
0.80	0.3056 ± 0.0080	$\textbf{0.1644} \pm \textbf{0.0082}$	$\textbf{0.7282} \pm \textbf{0.0136}$
0.90	0.3133 ± 0.0034	0.1834 ± 0.0035	0.6970 ± 0.0057
1.00	0.3136 ± 0.0183	0.1798 ± 0.0156	0.7028 ± 0.0257

Table 2: Layers and ρ_{max} vs. performance on CycPeptMPDB.

3.3.2 Causal Invariance under Re-batching

Setup as intervention. To evaluate the robustness of the learned representations under distributional shifts, we treat the test-time batch setup as an intervention variable. We fix the trained model and *intervene* on the test-time environment E by changing how the same test examples are partitioned into mini-batches: E = (B, shuffle) with $B \in \{8, 16, 32\}$ and with/without shuffling. This realizes do(E = e) that perturbs batch boundaries and co-occurrences while holding c(x) fixed. In the notation of Sec. 2.1, such interventions modify the batch-dependent context q(x, E) in the local predictor s(x, E) = ac(x) + bq(x, E) (Eq. equation 2) but leave the sample-intrinsic signal c(x) unchanged. Our learning mechanism (depth-wise correlation targets equation 6-equation 8) is designed to drive $b \to 0$, i.e., to make the causal readout rely on c(x) and be invariant to do(E = e).

For each intervention we compute *global* correlations between c and y over the test set. The correlation—depth curves (Fig. 4) remain monotonic and track the anchors for all B and shuffling choices.

Table 3: Test R^2 under do(E) via re-batching.

	B=8	B=16	B=32
R^2 (no)	0.7172	0.7282	0.7219
R^2 (shuf)	0.7120	0.7165	0.7184

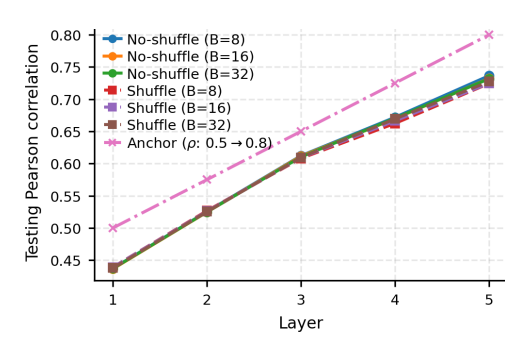


Figure 4: Environment interventions via rebatching.

(Table 3) Final-layer correlations lie in [0.7120, 0.7282] with total spread ≤ 0.0162 . Since interventions change E while keeping the examples fixed, this stability indicates that the learned alignment is insensitive to environment construction, as predicted by the batch-wise invariance principle supporting our claim that the predictor relies primarily on the sample-intrinsic component c(x).

3.3.3 PEELING DESIGN

We analyze how peeling depth L (number of causal blocks) and strength $\rho_{\rm max}$ (maximum target correlation) shape performance. Pushing either to extremes yields *under*- or *over*-peeling.

Peeling depth. We vary the number of causal blocks $L \in \{3,5,7,9\}$ and observe a U-shaped response in MAE/MSE and R^2 on CycPeptMPDB in the upper block of Table 2. With too few blocks (L=3), the hierarchy *under-peels*. It lacks capacity to progressively strip context, leaving causal and trivial signals entangled and hurting accuracy. With too many blocks (L=7,9), the hierarchy *over-peels*. The longer optimization path increases variance and can misroute label-relevant patterns into the trivial stream despite the monotonicity regularizer, degrading generalization. An interior optimum at L=5 aligns with a bias-variance view: depth must be large enough to separate signals but not so large that true causal evidence is shaved off together with context.

Peeling strength. We also examine the effect of the target-correlation parameter $\rho_{\max} \in \{0.60, 0.70, 0.80, 0.90, 1.00\}$ on CycPeptMPDB in the lower block of Table 2. Smaller targets (0.60-0.70) under-peel. The causal branch is not pushed hard enough, so contextual residue persists and errors rise. A moderate target (0.80) yields the best trade-off. Pursuing near-perfect within-batch correlation (0.90-1.00) over-peels. To satisfy an aggressive target, the model exploits batch-coupled features that should remain trivial, increasing variance and hurting generalization. Appendix A.3 provides additional evidence that an overly large target correlation causes context leakage.

3.4 CASE STUDY

Each causal block applies node-wise gating on atoms, producing $\alpha_i^{(\ell,m)} \in [0,1]$ for atom/group i in modality $m \in \{SM, PE, GE\}$ at depth ℓ . We take the final-layer weight as the causal score, $\pi_i^{(m)} = \alpha_i^{(L,m)} \in [0,1]$, and render causal saliency maps $\{\pi_i^{(m)}\}$ to inspect learned behavior.

Higher $\pi_i^{(m)}$ indicates atoms routed through the causal branch at the final layer. Figure 5 compares the under-peeling, optimal-peeling, and over-peeling settings. In the optimal case, saliency concentrates on chemically meaningful moieties, *consistent with chemical intuition*.

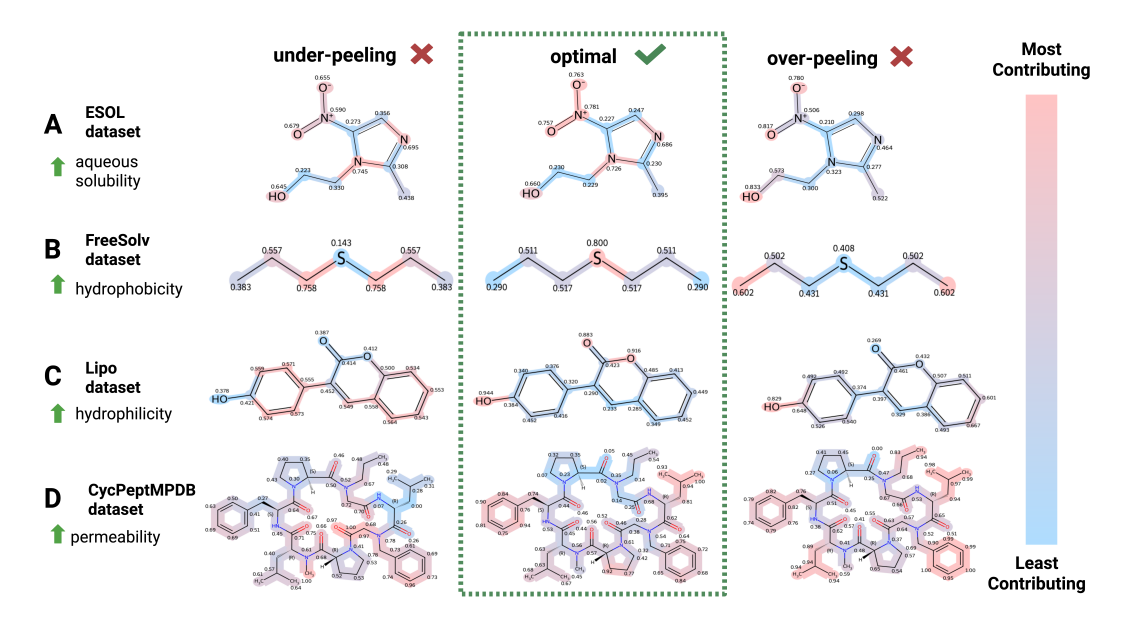


Figure 5: Layer-wise attribution maps in the multimodality setting across four benchmark datasets. Each row corresponds to a dataset and the molecular property of interest, indicated by the green arrow on the left. Three regimes are shown: under-peeling (left), optimal (center), and over-peeling (right). Atom-level contributions are highlighted with red atoms representing features most attributed to increasing the target property and blue atoms representing less contributing features. Optimal peeling yields clearer and more interpretable attribution compared to under- and over-peeling.

At the optimal depth, CLaP concentrates attribution on chemically coherent drivers per task.

In **A. ESOL dataset**, polar nitro groups and heteroatoms consistently dominate, reflecting their strong role in hydrogen bonding and aqueous solubility, especially in water.

In **B. FreeSolv dataset**, hydrocarbon segments together with the thio-linker carry the highest weights, consistently aligning with sulfur's tendency to raise local hydrophobicity and, consequently, the molecule's overall lipophilicity.

In **C. Lipo dataset**, the phenolic OH substituents and ring heteroatoms elevate hydrophilicity, while the extended aromatic surface is down-weighted, capturing the trade-off between polar handles and nonpolar bulk, consistent with established lipophilicity trends.

Finally, in **D.** CycPeptMPDB dataset, contiguous aromatic and aliphatic side chains form lipophilic patches that promote passive permeation, whereas backbone hydrogen-bond donors and acceptors contribute less, consistent with the desolvation cost of membrane crossing. This pattern reflects the intended peel—the shallow layers under-localize the signal, the deep layers over-peel and smear attribution, and the middle layers isolate chemically relevant substructures that drive the property.

4 RELATED WORK

Graph causal inference. Recent work aims to make graph predictors robust and interpretable by isolating label-relevant structure from spurious context. DIR selects invariant rationales (subgraphs that remain predictive across environments) and then predicts with the remainder (Wu et al., 2022). It depends on constructed environments from splits or augmentations, which can introduce artifacts not present in raw data. CIGA samples subgraphs with a learnable generator and enforces risk invariance with an information bottleneck (Chen et al., 2022). The sampling loop can slow and destabilize training, and a bias toward small subgraphs risks missing key components. For molecules, environment modeling adds or replaces functional groups and treats these variants as environments (Li et al., 2025), which may be chemically unfaithful and can widen the gap between training and test data even when raw data already mix causal and contextual factors. While CAL mitigates shortcuts and enhances interpretability (Sui et al., 2022), existing studies largely address classification. Regression is more challenging because the model must localize causal structure rather than exploit class-level artifacts. However, instead of crafting synthetic environments, our proposed CLaP achieves batchwise invariance via the natural mini-batch reshuffling that occurs during training, yielding stable within-batch correlations across depths and better causal capture under re-batching.

Molecular property prediction. Graph neural networks have become a cornerstone for molecular property prediction (Gilmer et al., 2017; Wu et al., 2018), achieving high accuracy on benchmarks by learning rich representations of molecular structures. Recent architectures extend beyond classical message passing: transformer-based models like the Molecule Attention Transformer incorporate geometric biases (inter-atomic distances) to capture 3D context (Maziarka et al., 2019), and multimodal frameworks fuse complementary inputs (e.g., chemical language and graphs) to further boost performance (Rollins et al., 2024). While these advances improve predictive power, they generally operate as black boxes and do not disentangle true causal factors from spurious correlations, limiting interpretability and their usefulness for guiding molecular design (Jiménez-Luna et al., 2020).

5 DISCUSSION

We presented CLaP, a layerwise causal—context peeling framework that realizes batch-wise invariance, improving predictive accuracy and delivering atom-level, chemically consistent explanations.

Looking ahead, this framework can expand in both scope and mechanics. Specifically, it extends beyond scalar regression to classification by swapping scalar label supervision for within-class correlation objectives, while preserving depthwise alignment. Furthermore, it is not confined to molecular graphs and can be embedded in transformer backbones to route tokens into causal and trivial paths, yielding token level causal maps across modalities and domains. These extensions aim to better capture underlying causal structure and enable more faithful problem analysis.

REPRODUCIBILITY STATEMENT

Implementation details and hyperparameters are in Appendix D.1. The supplementary material includes a code archive with configs, preprocessing, data loaders, architectures, and evaluations.

ETHICS STATEMENT

We adhere to ICLR Code of Ethics. No human subjects or personally identifiable data are involved. To reduce misuse risk, we release benchmarking code and models only for these datasets and provide no synthesis or activity oracles. No conflicts of interest or sensitive sponsorships are present.

REFERENCES

- Yoshua Bengio and Yann LeCun. Scaling learning algorithms towards AI. In *Large Scale Kernel Machines*. MIT Press, 2007.
- Hanxuan Cai, Huimin Zhang, Duancheng Zhao, Jingxing Wu, and Ling Wang. FP-GNN: a versatile deep learning architecture for enhanced molecular property prediction. *Briefings in Bioinformatics*, 23(6):12, 2022. doi: 10.1093/bib/bbac408.
- Yongqiang Chen, Yonggang Zhang, Yatao Bian, Han Yang, MA Kaili, Binghui Xie, Tongliang Liu, Bo Han, and James Cheng. Learning causally invariant representations for out-of-distribution generalization on graphs. *Advances in Neural Information Processing Systems*, 35:22131–22148, 2022.
- Robert Geirhos, Jörn-Henrik Jacobsen, Claudio Michaelis, Richard Zemel, Wieland Brendel, Matthias Bethge, and Felix A. Wichmann. Shortcut learning in deep neural networks. *Nature Machine Intelligence*, 2(11):665–673, 2020. doi: 10.1038/s42256-020-00257-z.
- Justin Gilmer, Samuel S. Schoenholz, Patrick F. Riley, Oriol Vinyals, and George E. Dahl. Neural message passing for quantum chemistry. In *Proceedings of the 34th International Conference on Machine Learning Volume 70*, ICML'17, pp. 1263–1272. JMLR.org, 2017.
- Ian Goodfellow, Yoshua Bengio, Aaron Courville, and Yoshua Bengio. *Deep learning*, volume 1. MIT Press, 2016.
- Geoffrey E. Hinton, Simon Osindero, and Yee Whye Teh. A fast learning algorithm for deep belief nets. *Neural Computation*, 18:1527–1554, 2006.
- José Jiménez-Luna, Francesca Grisoni, and Gisbert Schneider. Drug discovery with explainable artificial intelligence. *Nature Machine Intelligence*, 2(10):573–584, 2020. doi: 10.1038/s42256-020-00236-4.
- Limin Li, Kuo Yang, Wenjie Du, Pengkun Wang, Zhengyang Zhou, and Yang Wang. Soft causal learning for generalized molecule property prediction: An environment perspective. *arXiv* preprint arXiv:2505.06283, 2025.
- Łukasz Maziarka, Tomasz Danel, Sławomir Mucha, Krzysztof Rataj, Jacek Tabor, and Stanisław Jastrzębski. Molecule attention transformer. *Neural Information Processing Systems (NeurIPS)*, 2019.
- Zachary A. Rollins, Alan C. Cheng, and Essam Metwally. MolPROP: Molecular Property prediction with multimodal language and graph fusion. *Journal of Cheminformatics*, 16(1):56, 2024. doi: 10.1186/s13321-024-00846-9.
- Benjamin Sanchez-Lengeling and Alán Aspuru-Guzik. Inverse molecular design using machine learning: Generative models for matter engineering. *Science*, 361(6400):360–365, 2018. doi: 10.1126/science.aat2663.

- Yongduo Sui, Xiang Wang, Jiancan Wu, Min Lin, Xiangnan He, and Tat-Seng Chua. Causal attention for interpretable and generalizable graph classification. In *Proceedings of the 28th ACM SIGKDD Conference on Knowledge Discovery and Data Mining (KDD)*, pp. 1696–1705, 2022. doi: 10.1145/3534678.3539366.
- Yingxin Wu, Xiang Wang, An Zhang, Xiangnan He, and Tat-Seng Chua. Discovering invariant rationales for graph neural networks. In *Proceedings of the International Conference on Learning Representations (ICLR)*, 2022.
- Zhenqin Wu, Bharath Ramsundar, Evan N. Feinberg, Joseph Gomes, Caleb Geniesse, Apoorv S. Pappu, Karl Leswing, and Vijay Pande. Moleculenet: A benchmark for molecular machine learning. *Chemical Science*, 9:513–530, 2018. doi: 10.1039/C7SC02664A.
- Tianhong Zhang, Hongli Li, Hualin Xi, Robert V. Stanton, and Sergio H. Rotstein. Helm: a hierarchical notation language for complex biomolecule structure representation. *Journal of Chemical Information and Modeling*, 52(10):2796–2806, 2012. doi: 10.1021/ci3001925.

APPENDIX

A	The	oretical Analysis	13
	A.1	Batch-Wise Invariance Analysis	13
	A.2	Trivial Branch Analysis	14
	A.3	Target-Correlation Analysis	15
В	Add	itional Experiments	16
	B.1	Additional Ablation Study on Framework Design	16
	B.2	Multi-modality Design	17
	B.3	Cross-Modal Consistency	18
	B.4	Peeling Depth on Additional Datasets	19
C	Add	itional Case Studies and Multimodality Analysis	20
	C.1	ESOL Dataset	20
	C.2	FreeSolv Dataset	22
	C.3	Lipo Dataset	24
	C.4	CycPeptMPDB Dataset	26
D	Imp	lementation Details	28
	D.1	Proposed Framework Implementation Details	28
	D.2	Baselines Implementation Details	28
E	The	Use of Large Language Models (LLMs)	28

A THEORETICAL ANALYSIS

A.1 BATCH-WISE INVARIANCE ANALYSIS

We use the batch-centered correlation in Eq. equation 3 and the local form s(x, e) = a c(x) + b q(x, e) in Eq. equation 2. Define within-batch moments

$$\sigma_{c,e}^2 = \operatorname{Var}_e(c), \quad \sigma_{q,e}^2 = \operatorname{Var}_e(q), \quad \sigma_{y,e}^2 = \operatorname{Var}_e(y),$$
 $\kappa = \operatorname{Corr}_e(c, y), \quad \alpha_e = \operatorname{Corr}_e(q, y), \quad \rho_e = \operatorname{Corr}_e(c, q)$

with κ constant in e by (A1). Set

$$A_e = a \, \sigma_{c,e}, \qquad B_e = b \, \sigma_{q,e}.$$

Closed form for $Corr_e(s, y)$. Starting from the definition,

$$\operatorname{Corr}_{e}(s,y) = \frac{\operatorname{Cov}_{e}(s,y)}{\sqrt{\operatorname{Var}_{e}(s)\operatorname{Var}_{e}(y)}} \\
= \frac{\operatorname{Cov}_{e}(ac+bq,y)}{\sqrt{\operatorname{Var}_{e}(ac+bq)\operatorname{Var}_{e}(y)}} \\
= \frac{a\operatorname{Cov}_{e}(c,y) + b\operatorname{Cov}_{e}(q,y)}{\sqrt{\operatorname{Var}_{e}(ac+bq)}\sqrt{\operatorname{Var}_{e}(y)}} \\
= \frac{a\sigma_{c,e}\sigma_{y,e}\kappa + b\sigma_{q,e}\sigma_{y,e}\alpha_{e}}{\sqrt{a^{2}\sigma_{c,e}^{2} + b^{2}\sigma_{q,e}^{2} + 2ab\sigma_{c,e}\sigma_{q,e}\rho_{e}}\sigma_{y,e}} \quad \left(\operatorname{Cov}_{e}(u,v) = \sigma_{u,e}\sigma_{v,e}\operatorname{Corr}_{e}(u,v)\right) \\
= \frac{A_{e}\kappa + B_{e}\alpha_{e}}{\sqrt{A_{c}^{2} + B_{c}^{2} + 2A_{e}B_{e}\rho_{e}}} =: \frac{A_{e}\kappa + B_{e}\alpha_{e}}{D_{e}}. \tag{14}$$

Here $D_e = \sqrt{A_e^2 + B_e^2 + 2A_eB_e\rho_e} = \sigma_{s,e} > 0$ is the within-batch standard deviation of s.

A monotonicity observation ($\partial_{\alpha_e} \text{Corr}_e$). For fixed e, A_e , B_e , ρ_e do not depend on α_e , hence from equation 14

$$\frac{\partial}{\partial \alpha_e} \operatorname{Corr}_e(s, y) = \frac{\partial}{\partial \alpha_e} \frac{A_e \kappa + B_e \alpha_e}{D_e} = \frac{B_e}{D_e}.$$
 (15)

Therefore if $B_e \neq 0$ (equivalently $b \neq 0$), $Corr_e(s, y)$ is strictly monotone in α_e .

Consequence under exact invariance ($\operatorname{Corr}_{e_1} = \operatorname{Corr}_{e_2}$). Assume there exist batches e_1, e_2 with $\sigma_{c,e_1} = \sigma_{c,e_2}$, $\sigma_{q,e_1} = \sigma_{q,e_2}$, $\rho_{e_1} = \rho_{e_2}$, but $\alpha_{e_1} \neq \alpha_{e_2}$. Then $A_{e_1} = A_{e_2}$, $B_{e_1} = B_{e_2}$, $D_{e_1} = D_{e_2}$, and

$$\operatorname{Corr}_{e_1}(s, y) - \operatorname{Corr}_{e_2}(s, y) = \frac{B_{e_1}}{D_{e_1}} (\alpha_{e_1} - \alpha_{e_2}).$$

If $\operatorname{Corr}_e(s,y)$ is identical across batches (zero dispersion in Eq. equation 4), the right-hand side must be 0. Since $\alpha_{e_1} \neq \alpha_{e_2}$, this forces $B_{e_1} = 0$, hence b = 0 because $\sigma_{q,e_1} > 0$ by (A3).

Approximate invariance via a first-order expansion. Let $\delta_e(b) := \operatorname{Corr}_e(s,y) - \rho$, where ρ is the target in Eq. equation 4. Write $\operatorname{Corr}_e(s,y) = \Phi_e(B_e)$ with $\Phi_e(B) = \frac{A_e \kappa + B \alpha_e}{\sqrt{A_e^2 + B^2 + 2 A_e B \rho_e}}$. By the quotient rule,

$$\Phi'_e(B) = \frac{\alpha_e D_e - (A_e \kappa + B \alpha_e) D'_e}{D_e^2}, \qquad D'_e = \frac{B + A_e \rho_e}{D_e}.$$

Evaluating at B=0 (so $D_e=|A_e|$) gives

$$\left. \frac{\partial}{\partial B} \operatorname{Corr}_{e}(s, y) \right|_{B=0} = \Phi'_{e}(0) = \frac{\alpha_{e} A_{e}^{2} - A_{e} \kappa (A_{e} \rho_{e})}{|A_{e}|^{3}} = \frac{\alpha_{e} - \kappa \rho_{e}}{|A_{e}|}.$$
(16)

Since $B_e = b \, \sigma_{q,e}$, the chain rule yields

$$\left. \frac{\partial}{\partial b} \operatorname{Corr}_{e}(s, y) \right|_{b=0} = \sigma_{q, e} \left. \frac{\partial}{\partial B} \operatorname{Corr}_{e}(s, y) \right|_{B=0} = \frac{\sigma_{q, e}}{|A_{e}|} \left(\alpha_{e} - \kappa \rho_{e} \right). \tag{17}$$

Therefore, for small b,

$$\delta_e(b) = \delta_e(0) + b \Gamma_e + o(b), \qquad \Gamma_e = \frac{\sigma_{q,e}}{|A_e|} \left(\alpha_e - \kappa \rho_e \right). \tag{18}$$

If $\sum_e \Gamma_e^2 > 0$ (which holds whenever α_e varies across batches by (A2) and q is not batchwise collinear with c), minimizing the dispersion surrogate $\sum_e \delta_e(b)^2$ in Eq. equation 5 yields the closed-form

$$b^* = -\frac{\sum_e \delta_e(0) \Gamma_e}{\sum_e \Gamma_e^2} + o(1).$$
 (19)

Invariance conclusion. At b = 0, from equation 14 we have

$$\operatorname{Corr}_e(s,y)\big|_{b=0} = \frac{A_e \kappa}{|A_e|}, \quad \Rightarrow \quad \delta_e(0) = \frac{A_e \kappa}{|A_e|} - \rho.$$

With the natural choice $\rho = \kappa$ and $a \ge 0$ (so $A_e \ge 0$), we get $\delta_e(0) = 0$ for all e. Moreover, from equation 18 at b^\star we have $\delta_e(b^\star) = b^\star \Gamma_e + r_e(b^\star)$ with $\sum_e r_e(b^\star)^2 = o((b^\star)^2)$. Taking the ℓ_2 -norm and using Cauchy–Schwarz,

$$|b^{\star}| \|\Gamma\|_{2} \leq \|\delta(b^{\star})\|_{2} + \|r(b^{\star})\|_{2} = o(|b^{\star}|),$$

and since $\|\Gamma\|_2 > 0$ by (A2)–(A3), it follows that $b^* \Rightarrow 0$ as the model gradually reduces the contribution of the trivial component. Hence in the limit the predictor discards the batch-dependent q (i.e., $b^* \Rightarrow 0$ so $s \approx a c$), so

$$\operatorname{Corr}_{e}(s, y) \approx \operatorname{Corr}_{e}(c, y) = \kappa$$
 for all e .

A.2 TRIVIAL BRANCH ANALYSIS

With squared loss and the stop-gradient in Eq. equation 11, training t treats y_c^* as a constant with respect to its parameters, so the trivial head solves the conditional least-squares problem

$$t^{\star}(x) = \arg\min_{t} \mathbb{E}[(y - y_{c}^{\star} - t(x))^{2} \mid x] = \mathbb{E}[y - y_{c}^{\star} \mid x].$$

That is, the *best* residual correction at input x is the *conditional mean* of the residual.

Let $r := y - y_c^*$. By the definition of MSE risk $\mathcal{R}(f) = \mathbb{E}[(y - f(x))^2]$,

$$\mathcal{R}(y_c^{\star}) = \mathbb{E}[r^2].$$

Applying the Law of total expectation and conditional variance decomposition with $t \equiv 0$ gives the decomposition of the risk of y_c^* :

$$\mathcal{R}(y_{\mathrm{c}}^{\star}) = \mathbb{E}[r^2] = \mathbb{E}[\mathrm{Var}(r\mid x)] + \mathbb{E}[(\mathbb{E}[r\mid x])^2],$$

which splits the error into (i) irreducible noise $\mathbb{E}[\operatorname{Var}(r \mid x)]$ and (ii) predictable bias $\mathbb{E}[(\mathbb{E}[r \mid x])^2]$.

Plugging $t^*(x) = \mathbb{E}[r \mid x]$ into the predictor $\hat{y} = y_c^* + t$ removes the predictable bias:

$$\mathcal{R}(y_{\mathrm{c}}^{\star} + t^{\star}) = \mathbb{E}\Big[\mathrm{Var}(r\mid x) + (\mathbb{E}[r\mid x] - t^{\star}(x))^2\Big] \stackrel{t^{\star} = \mathbb{E}[r\mid x]}{=} \mathbb{E}\big[\mathrm{Var}(r\mid x)\big].$$

So adding t^{\star} strictly reduces risk by $\mathbb{E}[(\mathbb{E}[r\mid x])^2] \geq 0$ whenever the residual is partially predictable from x.

A.3 TARGET-CORRELATION ANALYSIS

Assume the additive label model

$$y = \theta c(x) + \eta, \qquad \mathbb{E}[\eta \mid x] = 0, \quad \text{Var}(\eta) > 0, \quad \theta \ge 0$$
 (20)

Then

$$Corr(c, y) = \frac{Cov(c, y)}{\sqrt{Var(c)Var(y)}} = \frac{\theta Var(c)}{\sqrt{Var(c)(\theta^2 Var(c) + Var(\eta))}} =: \kappa < 1.$$
 (21)

Any batch-invariant predictor using only c has s(x, e) = a c(x) and thus $Corr_e(s, y) = \kappa$ for all e.

Let s(x, e) = a c(x) + b q(x, e) as in Eq. equation 2, and define

$$\sigma_{c,e}^2 = \operatorname{Var}_e(c), \quad \sigma_{q,e}^2 = \operatorname{Var}_e(q), \quad \kappa = \operatorname{Corr}_e(c,y), \quad \alpha_e = \operatorname{Corr}_e(q,y), \ \rho_e = \operatorname{Corr}_e(c,q), \ A_e = a \ \sigma_{c,e}$$

From Eq. equation 14,

$$Corr_e(s,y) = \frac{A_e \kappa + b \sigma_{q,e} \alpha_e}{\sqrt{A_e^2 + b^2 \sigma_{q,e}^2 + 2A_e b \sigma_{q,e} \rho_e}}.$$

For the dispersion surrogate $\mathcal{L}_{\rho}(a,b) = \sum_{e} \left(\operatorname{Corr}_{e}(s,y) - \rho_{\star} \right)^{2}$ with target $\rho_{\star} \in (0,1)$, the first-order sensitivity at the invariant point b=0 is (Appendix A.1)

$$\left. \frac{\partial}{\partial b} \operatorname{Corr}_{e}(s, y) \right|_{b=0} = \frac{\sigma_{q, e}}{|A_{e}|} \left(\alpha_{e} - \kappa \, \rho_{e} \right) \; =: \; \Gamma_{e}, \qquad \left. \frac{\mathrm{d}}{\mathrm{d}b} \mathcal{L}_{\rho} \right|_{b=0} = 2(\kappa - \rho_{\star}) \sum_{e} \Gamma_{e}. \tag{22}$$

Under (A1)–(A3) and the mild non-collinearity $\exists e: \alpha_e \neq \kappa \rho_e$, the sum $\sum_e \Gamma_e$ is generically nonzero. If $\rho_\star > \kappa$ then $\kappa - \rho_\star < 0$, so $\mathrm{d}\mathcal{L}_\rho/\mathrm{d}b|_{b=0} \neq 0$ and b=0 is not a local minimizer. Hence any optimizer of \mathcal{L}_ρ satisfies |b|>0: the predictor must recruit the batch-dependent q(x,e) to reduce the surrogate when the target exceeds the invariant limit κ .

Moreover, writing $\delta_e(b) = \operatorname{Corr}_e(s, y) - \rho_{\star}$ and expanding at b = 0 gives

$$\delta_e(b) = (\kappa - \rho_{\star}) + b \Gamma_e + o(b), \quad \Rightarrow \quad b^{\star} = \frac{(\rho_{\star} - \kappa) \sum_e \Gamma_e}{\sum_e \Gamma_e^2} + o(1).$$

Thus the leakage magnitude grows linearly with the target gap $(\rho_{\star} - \kappa)$ and is controlled by the batch statistics through $\{\Gamma_e\}$.

B ADDITIONAL EXPERIMENTS

B.1 ADDITIONAL ABLATION STUDY ON FRAMEWORK DESIGN

Table 4: Additional ablation study on framework design across four datasets.

Setting	MAE	MSE	R^2	
ESOL				
CLaP	0.4456 ± 0.0151	0.3583 ± 0.0095	0.9157 ± 0.0022	
Average causal layer	0.4798 ± 0.0172	0.4377 ± 0.0064	0.8990 ± 0.0218	
No mono penalty	0.5692 ± 0.0192	0.5740 ± 0.0606	0.8600 ± 0.0165	
	Free	Solv		
CLaP	0.7020 ± 0.0044	0.8866 ± 0.0522	0.9160 ± 0.0049	
Average causal layer	0.9612 ± 0.0239	1.5843 ± 0.0435	0.8498 ± 0.0420	
No mono penalty	1.0241 ± 0.1422	1.7210 ± 0.3891	0.8368 ± 0.0369	
	Li	ро		
CLaP	0.4672 ± 0.0020	0.3645 ± 0.0274	0.7515 ± 0.0187	
Average causal layer	0.5621 ± 0.0124	0.5041 ± 0.0156	0.6563 ± 0.0016	
No mono penalty	0.5288 ± 0.0591	0.4590 ± 0.0845	0.6870 ± 0.0576	
CycPeptMPDB				
CLaP	0.3056 ± 0.0080	0.1644 ± 0.0082	0.7282 ± 0.0136	
Average causal layer	0.3227 ± 0.0118	0.1859 ± 0.0067	0.6943 ± 0.0160	
No mono penalty	0.3137 ± 0.0051	0.1803 ± 0.0032	0.7051 ± 0.0089	

w/o monotonicity constraint. The monotonicity penalty \mathcal{L}_{mono} (Eq. equation 9) complements the correlation loss by coupling adjacent depths, encouraging non-decreasing label-correlation as depth increases. This depthwise ordering regularizes training, especially for deeper causal blocks, by discouraging oscillations and preventing later layers from overwriting gains established earlier.

Ablating $\mathcal{L}_{\mathrm{mono}}$ weakens layerwise refinement of causal features, leading to a modest yet consistent performance drop. Monotonicity regularizer improves hierarchical stability and makes the layerwise specialization more reliable.

Average causal across layers. This ablation probes the depthwise correlation design. The targets $\{\rho_\ell\}$ increase with depth (Eq. equation 7) and, together with \mathcal{L}_{corr} and \mathcal{L}_{mono} (Eqs. equation 8, equation 9), train the deepest causal block to become progressively more label–relevant. Here we replace the final-layer causal output with a uniform average of $\{c^{(\ell)}\}_{\ell=1}^L$. Given $corr_1 \leq \cdots \leq corr_L$ under $\mathcal{L}_{corr} + \mathcal{L}_{mono}$, averaging $\bar{c} = \frac{1}{L} \sum_{\ell} c^{(\ell)}$ mixes in low-correlation early representations. For centered variables, $Corr(\bar{c}, y) \leq Corr(c^{(L)}, y)$, with strict inequality unless all $c^{(\ell)}$ are colinear with $c^{(L)}$. Thus using $c^{(L)}$ is theoretically favored.

In our experiments, averaging across layers undermines depthwise specialization and mixes early-layer representations that retain substantial context information into the final predictor, contaminating the causal signal and degrading performance (e.g., $R^2:0.728 \rightarrow 0.694$, MSE: $0.164 \rightarrow 0.185$). These results validate the design: the last causal layer concentrates the causal signal, while earlier layers serve as progressively coarser precursors.

Together, the correlation schedule shapes *what* each depth should capture; the monotonicity term enforces *how* the hierarchy evolves; the trivial branch determines *where* non-causal residuals go.

B.2 MULTI-MODALITY DESIGN

Table 5: Effect of causal peeling under unimodal vs. multimodal settings across four datasets.

Setting	MAE	MSE	R^2
	ESOL		
Multimodal			
w causal-trivial split	0.4456 ± 0.0151	0.3583 ± 0.0095	0.9157 ± 0.0022
w/o causal-trivial split	0.5094 ± 0.0528	0.4939 ± 0.1034	0.8838 ± 0.0243
2D Graph			
w causal-trivial split	0.9453 ± 0.0156	1.5993 ± 0.0719	0.6238 ± 0.0169
w/o causal-trivial split	0.9631 ± 0.0092	1.6931 ± 0.0817	0.6018 ± 0.0192
3D Geometry			
w causal-trivial split	0.5322 ± 0.0029	0.5235 ± 0.0268	0.8769 ± 0.0063
w/o causal-trivial split	0.5219 ± 0.0055	0.5036 ± 0.0088	0.8816 ± 0.0021
	FreeSol	v	
Multimodal			
w causal-trivial split	$\textbf{0.7020} \pm \textbf{0.0044}$	0.8866 ± 0.0522	0.9160 ± 0.0049
w/o causal-trivial split	1.2858 ± 0.2120	2.5719 ± 0.8194	0.7562 ± 0.0777
2D Graph			
w causal-trivial split	1.1267 ± 0.0098	1.9876 ± 0.2791	0.8116 ± 0.0265
w/o causal-trivial split	1.2003 ± 0.0410	2.4157 ± 0.2852	0.7710 ± 0.0270
3D Geometry			
w causal-trivial split	1.0640 ± 0.0001	1.8055 ± 0.0591	0.8288 ± 0.0056
w/o causal-trivial split	1.0721 ± 0.0875	1.9262 ± 0.2170	0.8174 ± 0.0206
	Lipo		
Multimodal			
w causal-trivial split	$\textbf{0.4672} \pm \textbf{0.0021}$	0.3645 ± 0.0274	0.7515 ± 0.0187
w/o causal-trivial split	0.5145 ± 0.0425	0.4302 ± 0.0442	0.7067 ± 0.0381
2D Graph			
w causal-trivial split	0.5171 ± 0.0234	0.4506 ± 0.0424	0.6928 ± 0.0289
w/o causal-trivial split	0.5230 ± 0.0283	0.4504 ± 0.0411	0.6929 ± 0.0280
3D Geometry			
w causal-trivial split	0.6412 ± 0.0339	0.6519 ± 0.0784	0.5556 ± 0.0534
w/o causal-trivial split	0.6260 ± 0.0739	0.6449 ± 0.1567	0.5603 ± 0.1069
	CycPeptMI	PDB	
Multimodal			
w causal-trivial split	0.3056 ± 0.0080	$\textbf{0.1644} \pm \textbf{0.0082}$	0.7282 ± 0.0136
w/o causal-trivial split	0.3120 ± 0.0047	0.1834 ± 0.0063	0.6969 ± 0.0104
2D Graph			
w causal-trivial split	0.4068 ± 0.0001	0.2889 ± 0.0112	0.5226 ± 0.0184
w/o causal-trivial split	0.4077 ± 0.0069	0.2884 ± 0.0069	0.5234 ± 0.0114
HELM Notation			
w causal-trivial split	0.3310 ± 0.0034	0.2023 ± 0.0005	0.6657 ± 0.0008
w/o causal-trivial split	0.3194 ± 0.0026	0.1910 ± 0.0025	0.6843 ± 0.0042
3D Geometry			
w causal-trivial split	0.4221 ± 0.0111	0.3102 ± 0.0164	0.4874 ± 0.0271
w/o causal-trivial split	0.4244 ± 0.0087	0.3071 ± 0.0134	0.4924 ± 0.0222

In this section, we assess how the causal–trivial split behaves under different modality configurations. CycPeptMPDB provides three complementary views per sample (SM, PE, GE), whereas ESOL, FreeSolv, and Lipo provide two views (SM and GE). Table 5 compares unimodal variants with multimodal fusion, each trained with and without the split.

With two or more modalities, enabling the split generally yields better fit and stability across datasets. For instance, MSE decreases on CycPeptMPDB from 0.183 to 0.164 and on ESOL from 0.494 to 0.358, with similar gains on FreeSolv and Lipo. This pattern aligns with Sec. 2.2. After node and edge splitting, the depthwise gate $\boldsymbol{w}^{(\ell)}$ emphasizes the modality whose causal branch carries batch invariant evidence. The correlation schedule aligns each layer's causal scalar with the label, and the residual path learns remaining context with a stop gradient to prevent leakage into the causal branch. Fusion supplies complementary cues that the curriculum can promote and confounding that it can peel away, which strengthens accuracy.

Algorithm 1: Layer-wise causal-trivial peeling

```
Input: multi-view data (x_{SM}, x_{PE}, x_{GE}) with label y; depth L; epochs E; batch size B;
            correlation targets \{\rho_{\ell}\}; weights \lambda_{\text{caus}}, \lambda_{\text{mono}}, \lambda_{\text{unif}}.
Output: trained predictor \hat{y} = c^* + t.
```

for e = 1 to E do

for each mini-batch do

Encode inputs into embeddings.

for $\ell = 1$ to L do

Split into causal/trivial parts, fuse across modalities, get scalars $c^{(\ell)}, t^{(\ell)}$.

 $\begin{array}{ll} c^{\star} \leftarrow \boldsymbol{c}^{(L)}, & t \leftarrow \sum_{\ell} \boldsymbol{t}^{(L)}, & \widehat{y} \leftarrow c^{\star} + t. \\ \text{Compute losses: } \mathcal{L}_{\text{pred}} \text{ (MSE)}, \mathcal{L}_{\text{corr}} \text{ (correlation)}, \mathcal{L}_{\text{mono}} \text{ (monotonicity)}, \mathcal{L}_{\text{triv}} \end{array}$

 $\text{Total: } \mathcal{L}_{\mathrm{total}} = \mathcal{L}_{\mathrm{pred}} + \lambda_{\mathrm{caus}} \mathcal{L}_{\mathrm{corr}} + \lambda_{\mathrm{mono}} \mathcal{L}_{\mathrm{mono}} + \lambda_{\mathrm{unif}} \mathcal{L}_{\mathrm{triv}};$ optimizer step w.r.t. $\nabla \mathcal{L}_{\text{total}}$.

For single view variants, changes are small or mixed. ESOL based on 2D shows a modest R^2 gain from 0.602 to 0.624, while ESOL based on 3D declines slightly from 0.882 to 0.877. Lipo based on 2D is essentially unchanged at about 0.693, whereas Lipo based on 3D decreases a bit from 0.560 to 0.556. On CycPeptMPDB, 2D and 3D are near ties and HELM drops from 0.684 to 0.666. FreeSolv is an exception where single view 2D and 3D both improve to 0.812 and 0.829. In practice, single view deployments use a milder target schedule or omit the split while retaining residual calibration. The split functions best as a fusion amplifier when depthwise correlation guidance and cross modal gating can reinforce each other.

B.3 CROSS-MODAL CONSISTENCY

Table 6: Effect of consistency weight across datasets.

Setting	MAE	MSE	R^2		
	ESOL				
CLaP	0.4456 ± 0.0151	0.3583 ± 0.0095	0.9157 ± 0.0022		
$\lambda_{\rm cons} = 0.5$	0.5242 ± 0.0618	0.5106 ± 0.1179	0.8799 ± 0.0277		
$\lambda_{\rm cons} = 1.0$	0.5192 ± 0.0439	0.5050 ± 0.0583	0.8812 ± 0.0137		
		FreeSolv			
CLaP	0.7020 ± 0.0044	0.8866 ± 0.0522	0.9160 ± 0.0049		
$\lambda_{\rm cons} = 0.5$	1.0550 ± 0.3457	1.8375 ± 1.0257	0.8258 ± 0.0972		
$\lambda_{\rm cons} = 1.0$	1.1412 ± 0.2175	2.0513 ± 0.7842	0.8055 ± 0.0743		
		Lipo			
CLaP	0.4672 ± 0.0201	0.3645 ± 0.0274	0.7515 ± 0.0187		
$\lambda_{\rm cons} = 0.5$	0.5649 ± 0.0272	0.5002 ± 0.0496	0.6899 ± 0.0338		
$\lambda_{\rm cons} = 1.0$	0.5597 ± 0.0920	0.4949 ± 0.1213	0.6626 ± 0.0827		
CycPeptMPDB					
CLaP	0.3056 ± 0.0080	0.1644 ± 0.0082	0.7282 ± 0.0136		
$\lambda_{\rm cons} = 0.5$	0.3204 ± 0.0002	0.1934 ± 0.0097	0.6803 ± 0.0160		
$\lambda_{\rm cons} = 1.0$	0.3154 ± 0.0015	0.1839 ± 0.0012	0.6960 ± 0.0020		

We vary a cosine-similarity penalty between modality-specific embeddings with weight $\lambda_{\rm cons}$ to test whether enforcing cross-modal agreement helps or hurts (Table 6). Across datasets, adding this penalty degrades the metrics compared to our default, with larger weights producing larger drops. The effect is most visible on FreeSolv and Lipo, and still present on CycPeptMPDB and ESOL.

This pattern is consistent with our design in Sec. 2.2. The model benefits from complementarity across modalities: the split routes label-relevant signal to the causal branch while the fusion gate selects the modality that carries the most batch-invariant evidence at each depth. Forcing embeddings to be too similar collapses modality-specific subspaces, reduces the gate's effective choice set, and makes batch-coupled shortcuts more likely to be shared. The correlation curriculum then has less diverse causal evidence to promote, and the residual path absorbs less of the confounding context. In practice, we keep λ_{cons} at zero or very small to preserve complementarity.

B.4 PEELING DEPTH ON ADDITIONAL DATASETS

Table 7: Peeling depth ablation on ESOL, FreeSolv, and Lipo.

Layer	MAE	MSE	R^2
		ESOL	
1	0.4879 ± 0.0098	0.4293 ± 0.0101	0.8990 ± 0.0024
2	0.4456 ± 0.0151	0.3583 ± 0.0095	0.9157 ± 0.0022
3	0.5495 ± 0.1119	0.5794 ± 0.2043	0.8637 ± 0.0565
4	0.5463 ± 0.0235	0.5335 ± 0.0234	0.8745 ± 0.0055
		FreeSolv	
1	0.9733 ± 0.1168	1.9424 ± 0.1979	0.8159 ± 0.0188
2	0.7020 ± 0.0044	0.8866 ± 0.0522	0.9160 ± 0.0049
3	0.8987 ± 0.0910	1.4897 ± 0.3848	0.8588 ± 0.0365
4	0.9849 ± 0.0834	1.5328 ± 1.1299	0.8547 ± 0.0123
		Lipo	
1	0.5201 ± 0.0347	0.4506 ± 0.0626	0.6928 ± 0.0427
2	0.5079 ± 0.0504	0.4356 ± 0.0676	0.7030 ± 0.0461
3	0.4672 ± 0.0201	0.3645 ± 0.0274	0.7515 ± 0.0187
4	0.5376 ± 0.0366	0.4699 ± 0.0455	0.6796 ± 0.0310

We extend the depth sweep to the remaining datasets. Table 7 shows a consistent U-shaped trend as the number of causal blocks increases. With too few layers the hierarchy *under-peels*. As depth grows beyond a dataset-dependent sweet spot the hierarchy *over-peels*.

ESOL and FreeSolv favor shallow hierarchies (two causal blocks), whereas Lipo benefits from one additional block, likely due to greater dataset complexity. This pattern is consistent with bias-variance tradeoffs and batch-wise invariance objective. The additional layer is useful when it tries to capture more complex signal.

In practice, we select depth by monitoring the layerwise correlation curve against the target schedule and choosing the smallest L at which the validation error reaches its first stable minimum while correlations remain monotone and close to the anchors. Beyond that point additional layers yield diminishing returns and increase sensitivity to context.

C ADDITIONAL CASE STUDIES AND MULTIMODALITY ANALYSIS

C.1 ESOL DATASET

We benchmark on the ESOL dataset, which contains 1128 small organic molecules with experimentally measured aqueous solubility reported as

$$\log S \equiv \log_{10} (\text{molar solubility in water (mol/L)}).$$

Thus, the sign directly encodes scale: positive values mean solubility > 1 mol/L, $\log S = 0$ corresponds to 1 mol/L, and negative values mean solubility < 1 mol/L.

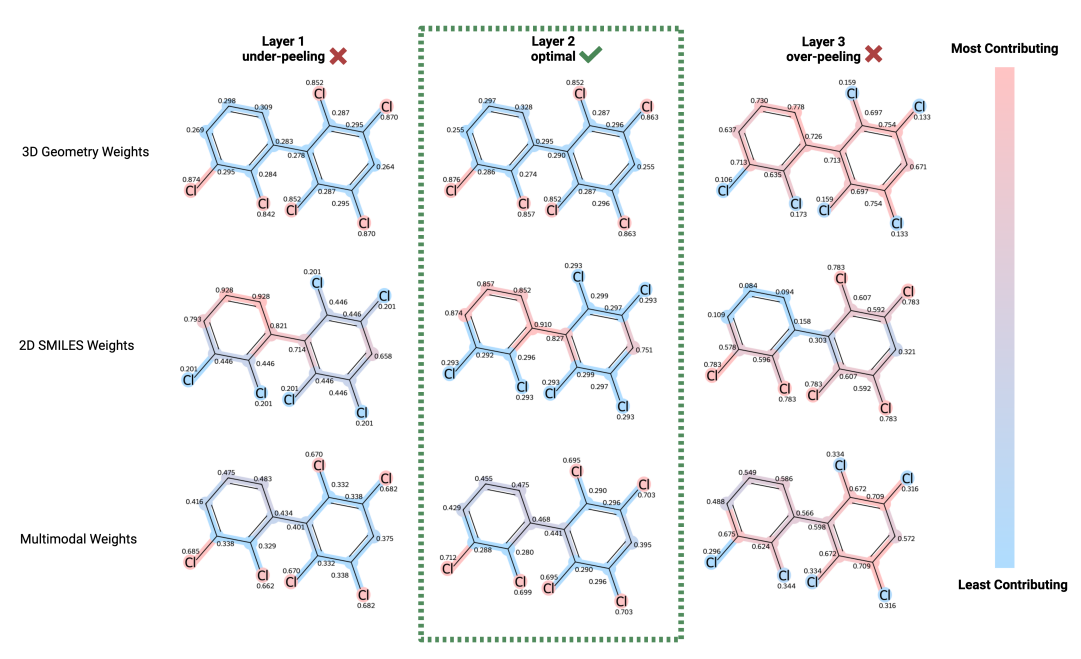


Figure 6: Layer-wise attribution maps across input modalities. Red colored atoms are attributed with affecting the molecule's water affinity the most.

At the optimal depth (L2), CLaP assigns the highest weights to chloro substituents and adjacent aryl carbons that cluster via short Cl–C/Cl–Cl distances in 3D; the fused readout preserves this through-space signal while the 2D branch highlights halogenated positions from connectivity alone. This depth-wise focus is exactly the intended "peel": batch-coupled context is removed, and label-relevant structure (a single hydrophobic patch) is retained. The outcome matches physical chemistry: contiguous chlorination increases non-polar surface and reduces hydrogen-bonding capacity, driving logS lower. Under-peeling spreads attribution across the ring (shortcuts), and over-peeling reintroduces residual context, illustrating why CLaP's layerwise schedule matters.

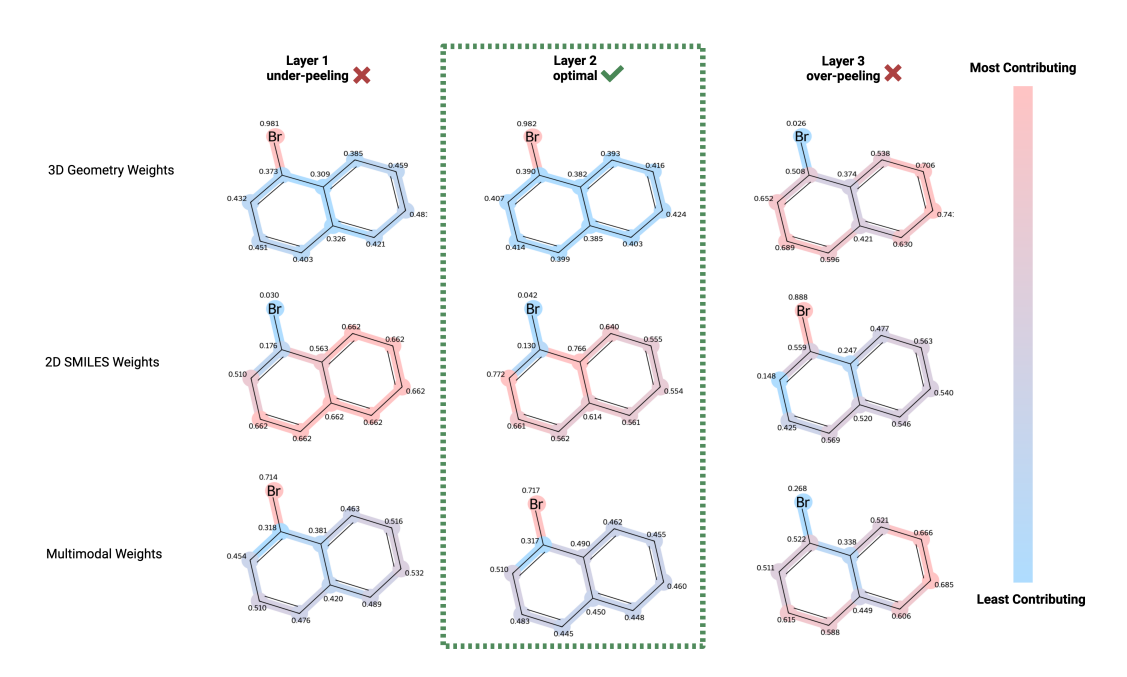


Figure 7: Layer-wise attribution maps across input modalities. Red colored atoms are attributed with affecting the molecule's insolubility the most.

At the optimal depth (L2), CLaP assigns the highest weights to the *aryl bromide* and the *fused bicyclic ring junction*; the 3D branch aggregates the planar π -surface into a single hydrophobic patch, while the 2D branch captures bromination and ring fusion from connectivity alone. This depth-wise focus is exactly the intended "peel": batch-coupled context is removed, and label-relevant structure (a large, contiguous hydrophobic surface) is retained. The outcome matches physical chemistry: expanded aryl surface together with Br increases lipophilicity and contributes essentially no hydrogen-bond donors/acceptors, yielding minimal polar counterbalance and driving $\log S$ more negative (lower aqueous solubility). Under-peeling spreads attribution across the scaffold (shortcuts), and over-peeling smears weights and reintroduces residual context. CLaP effectively captures a general rule in physical chemistry: addition of halogen groups increases the molecule's overall solubility in organic solvents and decreases the molecule's overall solubility in aqueous solvents.

C.2 FREESOLV DATASET

We benchmark on the FreeSolv dataset, which contains 642 small organic molecules with experimentally measured hydration free energies in water reported as

$$\Delta G_{\text{hvd}}$$
 [kcal/mol].

Thus, the sign directly encodes favorability: *negative* values mean exergonic (favorable) hydration and greater water affinity, values near 0 indicate weak preference, and *positive* values mean endergonic (unfavorable) hydration and greater hydrophobicity.

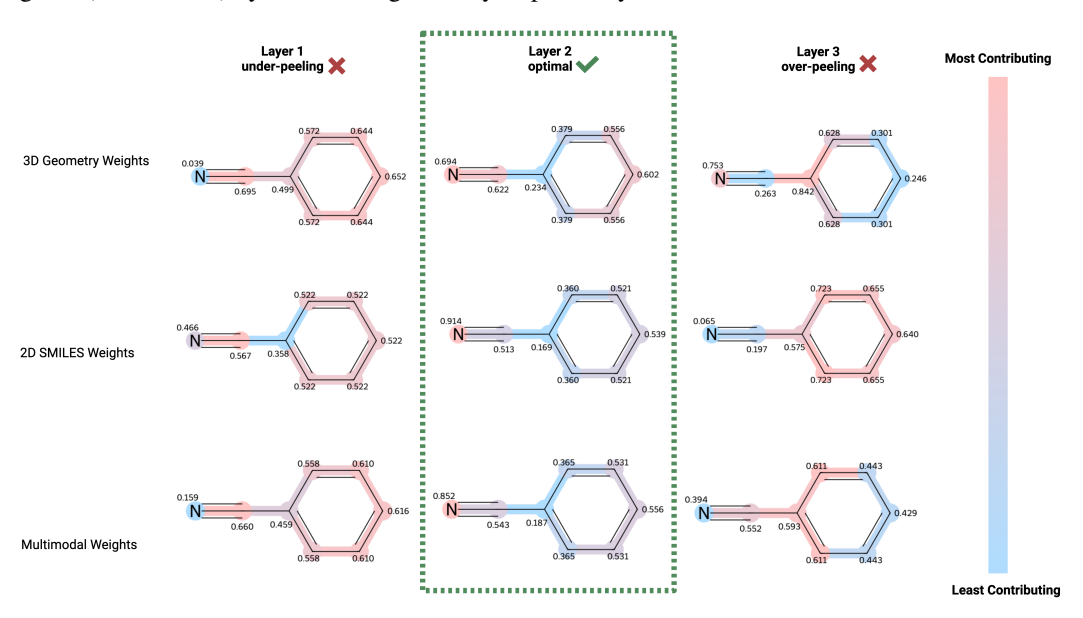


Figure 8: Layer-wise attribution maps across input modalities. Red colored atoms are attributed with affecting the molecule's hydrophilicity the most.

At the optimal depth (L2), CLaP assigns the highest weights to the *nitrile substituent* and the adjacent aromatic carbons; the 3D branch aggregates the linear C \equiv N dipole into a localized polar feature, while the 2D branch captures the nitrile group and ring context from connectivity. This depth-wise focus is exactly the intended "peel": batch-coupled context is removed, and label-relevant structure (a polar handle appended to an aryl surface) is retained. The outcome matches physical chemistry: the nitrile increases polarity and provides a strong dipole acceptor, raising aqueous solubility relative to an unsubstituted aryl. Nitriles are widely used in medicinal chemistry contexts as metabolically stable polar groups that tune solubility and binding while maintaining a compact scaffold.

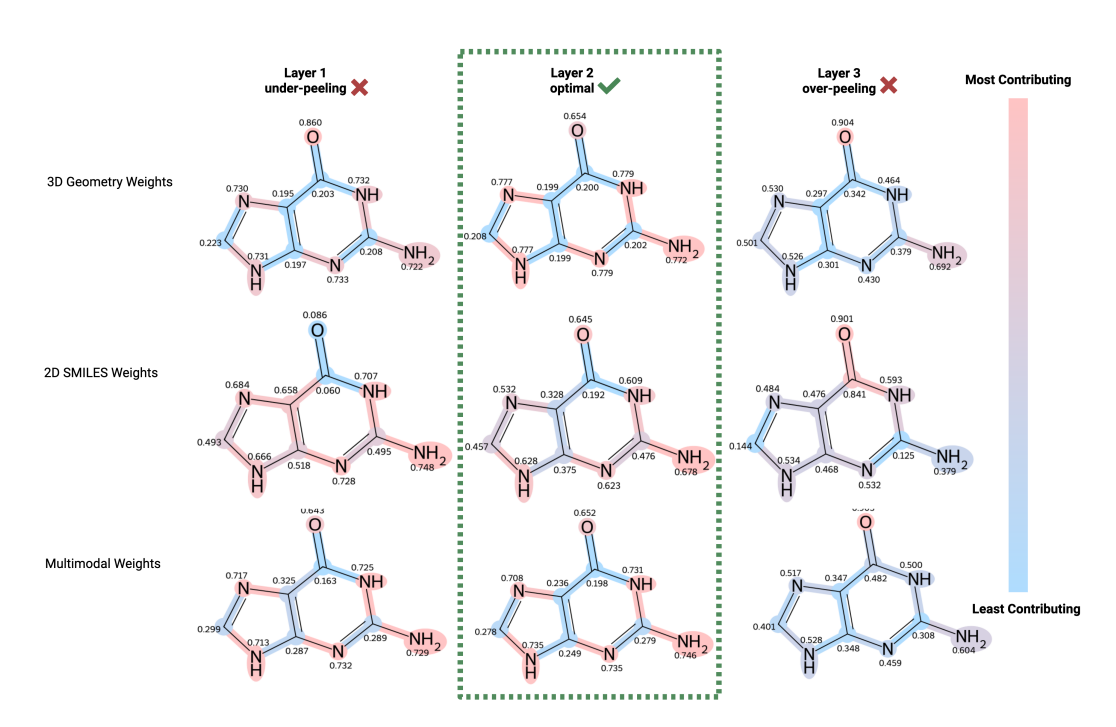


Figure 9: Layer-wise attribution maps across input modalities. Red colored atoms are attributed with affecting the molecule's hydrophilicity the most.

At the optimal depth (L2), CLaP assigns the highest weights to the *carbonyl oxygen* and the *exocyclic amine group*, with additional contributions from the ring nitrogens. The 3D branch aggregates the localized dipoles into a polar spine, while the 2D branch captures the carbonyl and amino substituents from connectivity. This matches physical chemistry: the carbonyl oxygen and multiple NH₂/NH groups provide hydrogen-bond acceptors and donors, substantially raising aqueous solubility relative to a purely carbocyclic core. Under-peeling diffuses weights across the ring scaffold (shortcuts), while over-peeling smears attribution and reintroduces residual context. Heteroaryl amides of this type are commonly found in nucleobases and drug-like scaffolds, where their balance of hydrogen-bonding capacity and planarity helps tune solubility in chemical biology.

C.3 LIPO DATASET

We benchmark on the Lipophilicity (Lipo) dataset which contains 4,200 small molecules curated experimentally. The target is the octanol/water distribution coefficient at physiological pH ($\log D_{7.4}$), defined as

 $\log D_{7.4} \, \equiv \, \log_{10} \biggl(\frac{[C]_{\rm octanol}}{[C]_{\rm water}} \biggr)_{\rm pH=7.4} \, , \label{eq:D7.4}$

where concentrations include all ionization states at pH 7.4. Thus, higher (more positive) $\log D_{7.4}$ denotes greater lipophilicity (preference for octanol), whereas lower/negative values indicate greater hydrophilicity.

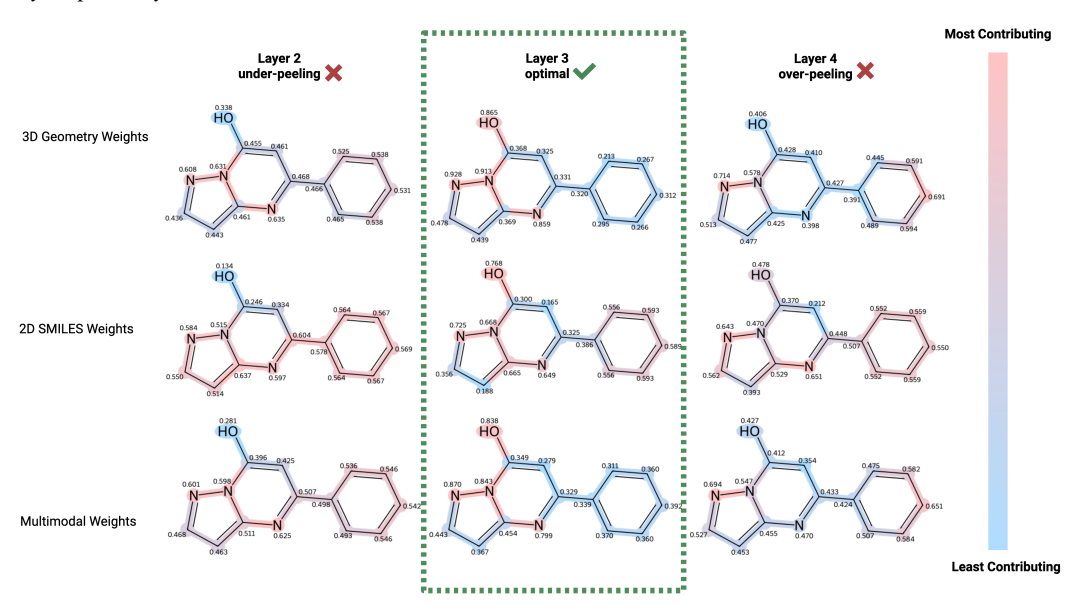


Figure 10: Layer-wise attribution maps across input modalities. Red colored atoms are attributed with affecting the molecule's hydrophilicity the most.

At the optimal depth (L3), CLaP assigns the highest weights to the *hydroxyl substituent* and nearby heteroaryl nitrogens. The 3D branch aggregates the O–H dipole into a localized polar hotspot, while the 2D branch highlights the hydroxyl group and its attachment point to the heteroaromatic ring. This depth-wise focus is exactly the intended "peel": batch-coupled context is removed, and label-relevant structure (polar donors/acceptors distributed across a largely aromatic scaffold) is retained. The outcome matches physical chemistry: the hydroxyl provides a strong hydrogen-bond donor and acceptor site, partially counterbalancing the extended aromatic surface. As a result, the molecule is predicted to be more *hydrophilic* than a fully unsubstituted aromatic analog.

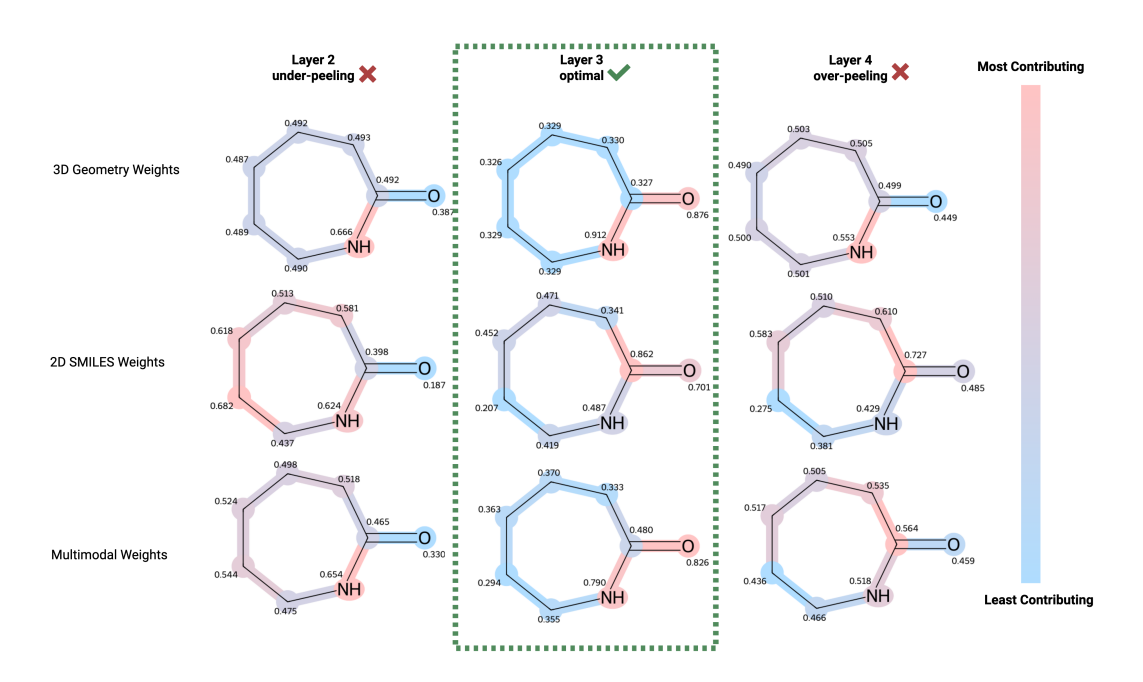


Figure 11: Layer-wise attribution maps across input modalities. Red colored atoms are attributed with affecting the molecule's hydrophilicity the most.

At the optimal depth (L3), CLaP assigns the highest weight to the *amide carbonyl oxygen* and the nearby amide nitrogen. The 3D branch captures the strong local dipole between the C=O and NH, while the 2D branch highlights the amide linkage from connectivity. This depth-wise focus is exactly the intended "peel": batch-coupled context is removed, and label-relevant structure (a polar amide motif appended to a hydrophobic ring) is retained. CLaP captures a general modification in chemistry: the amide group generally introduces both a hydrogen-bond donor and acceptor, increasing polarity and reducing lipophilicity relative to an unsubstituted carbocyclic scaffold. As a result, the molecule is predicted to be more *hydrophilic* (lower $\log D_{7.4}$).

C.4 CYCPEPTMPDB DATASET

We benchmark on the CycPeptMPDB dataset, which contains 7,334 cyclic peptides with experimentally measured passive membrane permeability reported on a logarithmic scale as

$$\log P \equiv \log_{10} (P \text{ [cm/s]}).$$

Thus, higher (less negative) $\log P$ denotes more permeable peptides, whereas more negative values indicate poor permeability.

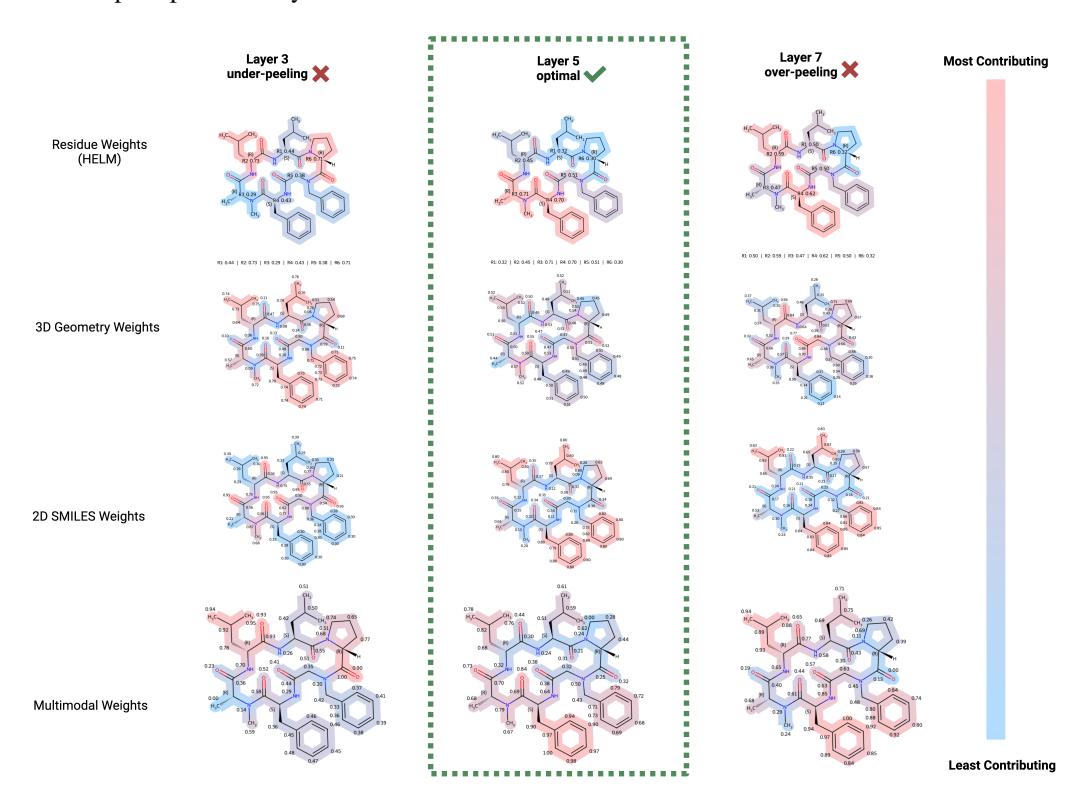


Figure 12: Layer-wise attribution maps across input modalities. Red colored atoms are attributed with affecting the molecule's permeability the most.

At the optimal depth (L5), CLaP highlights hydrophobic residues such as phenylalanine and aliphatic side chains as the dominant contributors. The 3D branch aggregates bulky aromatic surfaces into hydrophobic patches, while the HELM representation captures residue-level context. This depth-wise focus is exactly the intended "peel": batch-coupled noise is removed, and label-relevant features (hydrophobic residues that enhance membrane passage) are retained. The outcome is consistent with physical chemistry and with what is known for peptide therapeutics: aromatic and aliphatic substitutions increase lipophilicity and improve passive cell permeability. More broadly, such analyses underscore the drug-design logic of cyclic and linear peptide scaffolds: by balancing polarity (for solubility) with nonpolar residues (for permeability), peptide-based molecules can be optimized as potential drugs. Peptide drugs already play a major role in therapy, ranging from hormones and enzyme inhibitors to next-generation modulators of protein–protein interactions.

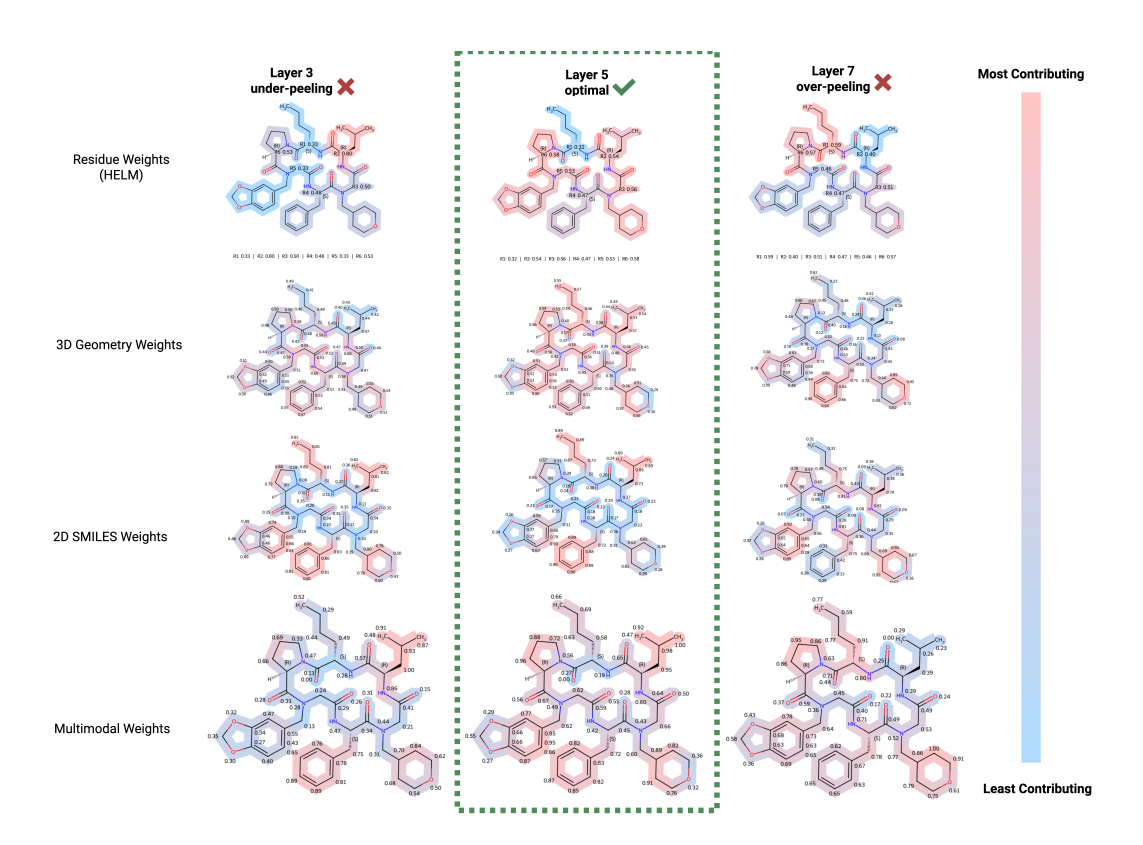


Figure 13: Layer-wise attribution maps across input modalities. Red colored atoms are attributed with affecting the molecule's permeability the most.

At the optimal depth (L5), CLaP again highlights hydrophobic residues such as aromatics and aliphatic side chains as the main drivers of permeability. These groups form contiguous lipophilic patches, favoring bilayer partitioning and consistent with design principles for permeable peptides. In contrast, heteroatom-rich sites such as oxygen incorporated cycles contribute less, reflecting their polarity and the desolvation penalty that reduces passive diffusion. Thus, the model recovers a chemically intuitive balance: hydrophobic groups increase permeability, while oxygen and general incorporation of polar atoms in the side chains reduce permeability. CLaP is able to distinguish both drivers of permeability, as well as identify motifs that harm permeability, suggesting molecular edits that chemists can make to optimize the peptide.

D IMPLEMENTATION DETAILS

D.1 PROPOSED FRAMEWORK IMPLEMENTATION DETAILS

For CycPeptMPDB, we encode 2D molecular graphs and HELM strings with GAT and 3D geometries with EGNN; each backbone has 3 layers, producing 128-D embeddings that are linearly projected to a shared 256-D space. The target correlation schedule increases linearly from 0.5 to 0.8 across L=5 causal blocks. Training runs for 100 epochs with batch size 16 on $8\times$ RTX-6000 GPUs with early stopping. Loss weights are $\lambda_{\rm caus}=1.0$, $\lambda_{\rm unif}=1.0$, and $\lambda_{\rm mono}=0.5$; cross-modal consistency is disabled ($\lambda_{\rm cons}=0$), and the hinge margin is set to 0. For ESOL, FreeSolv, and Lipo (non-peptide datasets), we use two modalities (2D graphs and 3D geometries); unless noted otherwise, embeddings are projected to 256-D and the correlation schedule is $0.4\rightarrow0.7$. ESOL uses width 128 with 2 encoder layers and L=2 causal blocks; FreeSolv uses width 64 with 2 layers and L=2; Lipo uses width 64 with 3 layers and L=3. The hinge margin is 0 for all settings.

D.2 BASELINES IMPLEMENTATION DETAILS

For causality-oriented baselines, we modified the original classification-based causal framework into regression models for molecular property prediction. Specifically, the classification head was replaced with a regression head by fixing the output layer dimension to one. At the data level, we replaced the original discrete datasets with SMILES-derived PyG graph structures labeled with continuous molecular properties (e.g., permeability, logD74). For evaluation, metrics were changed from accuracy/AUC to MSE, RMSE, MAE, and R². These modifications preserve the structural features of the original architecture while adapting it to our new regression tasks.

E THE USE OF LARGE LANGUAGE MODELS (LLMS)

We used an LLM solely for light editorial assistance (grammar, wording, and minor style). The LLM did not contribute ideas, methods, models, experiments, analyses, or decisions, and was not used to generate or label data or code. All scientific content is by the authors.